Multi-element-resolved electrochemical corrosion analysis. Part I. Dissolution behavior and passivity of amorphous $Fe_{50}Cr_{15}Mo_{14}C_{15}B_6$

J. Klemm [a], S.O. Klemm [a], M.J. Duarte [a], L. Rossrucker [a], K.J.J. Mayrhofer [a], F.U. Renner [a,b,*]

[a] Department of Interface Chemistry and Surface Engineering, Max-Planck Institut für Eisenforschung, Max-Planck-Straße 1, 40237 Düsseldorf, Germany
[b] Institute for Materials Research (IMO), Hasselt University, Wetenschapspark 1, 3590 Diepenbeek, Belgium

ARTICLE INFO

ABSTRACT

Multi-element dissolution analysis of amorphous $Fe_{50}Cr_{15}Mo_{14}C_{15}B_6$ in 0.1 M H_2SO_4 was investigated electrochemically and by coupled online mass spectrometry. We fully discuss the most important aspects of the application of the newly-developed methodology to study complex multi-elemental alloys. The resulting partial dissolution rates of Fe, Cr and Mo reflect the passive behavior and are compared to the measured total current density as function of time. The deviations between the added elemental dissolution currents and the measured total current density are discussed. Furthermore, the inferred growth of oxide thickness was correlated to results obtained from surface analysis.

© 2014 The Authors. Published by Elsevier Ltd. This is an open access article under the CC BY-NC-ND license (http://creativecommons.org/licenses/by-nc-nd/3.0/).

1. Introduction

The structural and compositional complexity in modern alloy systems allows for an extraordinary variety in mechanical or functional behavior, but also constitutes a major challenge in controlling properties, e.g. in respect of corrosion performance. In addition to the individual contribution of each of the constituent elements, also their interplay may be of a decisive role. Passivity as a macroscopic corrosion phenomena, for example, is provided by the formation of a protective Cr-enriched oxide layer on (Fe-based) stainless steel surfaces in reaction with the solution environment [1,2]. The film stability is enhanced for alloys with an additional content of Mo [1,3,4]. Additional alloying elements which optimize certain aspects in behavior may, on the contrary, also have negative effects. For instance dangerous pitting attacks may be triggered by MnS inclusions in steels [4].

Stable homogeneous passive films under steady-state conditions can be well characterized by ex-situ surface analysis. Nevertheless, the surface films will eventually change, for example to adapt to different surface potentials or to changes in the environment such as the solution pH. Also localized corrosion may occur despite a mostly stable passive surface. Following the elemental dissolution into the electrolyte may in such cases provide key complementary insight into the reaction mechanisms. Under steady-state conditions, a detailed solution analysis allows to distinguish elemental dissolution from other background reactions such as gas evolution. The coupling of an electrochemical cell with online chemical analysis of the electrolyte offers thus time-resolved dissolution analysis which is important in corrosion studies. Recently, this was successfully conducted on single-element or multi-element systems by several groups, including inductively coupled plasma mass spectrometry (ICP-MS) [5–9], ultraviolet–visible spectroscopy [10], or inductively coupled plasma optical emission spectrometry (ICP-OES) [11]. For instance Ogle and coworkers investigated the selective dissolution of austenitic stainless steels during cathodic and anodic pulses by ICP-OES coupling [11]. Our Institute recently developed a new micro-electrochemical cell which was coupled directly online to ICP-MS [5–7], allowing simultaneous electrochemical experiments to be performed. The detailed chemical and electrochemical response is decisive for the respective stability and applicability of structural as well as functional materials. Furthermore, electrochemical reactions will influence the detailed electric field across the electrochemical interface and potentially change the interface structure during the reaction, which renders a detailed knowledge of the dissolution behavior even more useful for many applications [12–15].

Even with additional information by advanced element analytics, the structural and chemical complexity of substrates including inhomogeneity such as precipitates or simply grain boundaries still renders it often difficult to understand the fundamental

* Corresponding author at: Institute for Materials Research (IMO), Hasselt University, Wetenschapspark 1, 3590 Diepenbeek, Belgium. Tel.: +32 11 26 8835.
E-mail address: frank.renner@uhasselt.be (F.U. Renner).

mechanisms of corrosion reactions or "applied" corrosion reactions such as surface etching [7]. Fundamental questions in electrochemistry are therefore often addressed with homogeneous single-element or binary single-crystal alloys. Extremely homogeneous, but disordered, amorphous alloys allow in contrast for fundamental investigations of materials with a complex multi-elemental composition. Bulk metallic glasses and amorphous steels have been therefore frequently scrutinized for their corrosion behavior [1,3,16–19]. Yet, the time- and element-resolved in-situ dissolution has not been followed in detail so far.

We have earlier presented element-resolved corrosion analysis of $Fe_{50}Cr_{15}Mo_{14}C_{15}B_6$ during potentiodynamic experiments including nanostructure analysis of the amorphous and derived nanocrystalline alloys by atom probe tomography (APT) [20]. The formation of percolated Cr-rich and of Mo-rich Cr-depleted phases was found to prominently control the corrosion behavior for the fully nanocrystalline material. Here we further analyze in more detail the corrosion behavior of the amorphous $Fe_{50}Cr_{15}Mo_{14}C_{15}B_6$ alloy based on stationary as well as potential step experiments. The formed passive oxide was further characterized by X-ray photoelectron spectroscopy (XPS) surface analysis and quantitatively correlated to the obtained electrochemical results.

2. Experimental

2.1. Sample preparation

Amorphous alloys with the nominal composition $Fe_{50}Cr_{15}Mo_{14}C_{15}B_6$ (at.%) were produced by arc melting in purified argon atmosphere and subsequent melt spinning with a Cu wheel speed of 40 m s^{-1}. Ribbons with a width of 2–3 mm and a thickness of about 50 μm were obtained.

The amorphous state was confirmed by X-ray diffraction (XRD) measurements and the microstructure was analyzed with APT as has been reported in a previous paper [20].

Prior to any electrochemical measurements or surface analysis, all samples were ion milled for 5 min with argon ions at 5 keV and tilting angle of 70° (Gatan Co., Ltd., Model 682 PECS) to remove the surface oxide layer formed after the sample production by melt-spinning.

2.2. Electrochemical measurements

Electrochemical measurements were performed in 0.1 M H_2SO_4 solution at ambient pressure and temperature using a micro-electrochemical scanning flow cell (SFC) [20] with a potentiostat (Gamry Reference 600). The SFC consists of a polymethylmethacrylate (PMMA) block with two channels in V-geometry (with an angle of 60° and a diameter of 1 mm) for electrolyte inlet and outlet. The cell has an opening at the tip (area 1.1 mm²) encircled with a silicone sealing that prevents electrolyte leakage. The cell can be pressed directly on any sample surface which is connected as working electrode. The counter electrode (0.3 mm graphite) is positioned in the electrolyte inlet channel whereas the reference electrode (Ag/AgCl, Metrohm GmbH) is placed in a side compartment of the electrolyte outlet to avoid any contaminations.

For experiments with gas purging (argon and oxygen, 5.0 purity), the two additional channels of the cell were purged with argon to shield the area around the sample surface. The electrolyte reservoir was purged at least 15 min before the measurement with argon or oxygen, respectively. For electrochemical measurements, the open circuit potential (OCP) was recorded for 600–1000 s followed by potentiodynamic sweep experiments or potentiostatic polarization experiments. Potentiodynamic sweeps were recorded in anodic direction with a scan rate of 2 mV s^{-1}. Potentiostatic

experiments were performed with stepwise potential changes, each for 600 s and 1000 s, respectively, and as a single experiment for 3600 s at 0.8 V. All potentials were referred to SHE.

For coupling experiments the electrolyte outlet of the SFC is connected to the ICP-MS (NexION 300X, Perkin Elmer). An internal standard ([89]Y, 10 ppb, mixing ratio 1:1) is injected in a Y-connector prior to the analytics. Electrolyte and internal standard flows (both 220 μL min^{-1}) are driven by a peristaltic pump. A detailed description of the setup can be found elsewhere [5].

ICP-MS measurements were performed with a dynamic reaction cell (DRC) equipped with methane (0.5 mL min^{-1}, purity 5.5), which was used to suppress molecular ions (ArO^+, ArC^+) that interfere with [52]Cr and [56]Fe signals. Compared to the analysis of minor isotopes, the limits of detection of major isotopes were increased approximately 50-fold by using the DRC. Transient signals of [56]Fe, [98]Mo and [52]Cr were recorded continuously with a dwell time of 50 ms and 10 sweeps per reading. Limits of quantification (in $ng L^{-1}$), defined as the 10-fold standard deviation for blank analysis, were found to be 44.6 ng L^{-1} for Fe, 30.3 ng L^{-1} for Cr, and 3.5 ng L^{-1} for Mo, respectively. The light elements boron and carbon have not been considered. Carbon is ubiquitous in the environment and therefore prone to cross contamination in ICP-MS. The obtained individual metal dissolution current densities $i_{Diss,Me}$ with Me = Fe, Cr, and Mo are then added to a total dissolution current density $i_{Diss,total}$ which is compared to the measured total electrical current density i_m as described below in detail.

2.3. XPS analysis

XPS experiments were performed with a PHI Quantum 2000 (Physical Instruments, USA) using a monochromated Al-K$_\alpha$ X-ray source with 25 W and 15 kV. For the measurements a spot size of $100 \times 100 \text{ μm}^2$ at 45° take-off angle was used. For high resolution detail spectra, the pass energy was set to 23.5 eV and the step size to 0.2 eV. Sputter depth profiles were recorded with an Ar ion sputter gun on an area of $1.5 \times 1.5 \text{ mm}^2$ with an acceleration voltage of 1 kV. The used sputter rate was approximately 1.33–1.68 nm min^{-1} determined using a SiO_2 standard. The time scale of the depth profiles was converted to sputter depth according to the determined sputter parameters.

XPS analysis was carried out on fresh ion milled samples, on samples held at OCP for 600 s and on samples polarized at 0.8 V_{SHE} for 3600 s in 0.1 M H_2SO_4. All samples were carefully rinsed with water and ethanol and dried with nitrogen before the measurements. The fitting of XPS sputter profiles was done using CasaXPS software. The spectra were referenced to the carbon C1s peak at 285.0 eV. The intensities of the peaks were converted to atomic concentration by using sensitivity factors provided by the manufacturer. The individual elemental intensities were normalized by assuming the presence of the bulk composition ($Fe_{50}Cr_{15}Mo_{14}C_{15}B_6$) at a sputter depth >9 nm. The film thickness was estimated using the depth at which the oxygen intensity reached half of the maximum, as used by several authors [2,21,22]. It is important to consider that the etch rates of Fe- and Cr-oxides differ from those of SiO_2 as reported for one example by Baer [23]. Because the surface films consist of mixed oxides and hydroxides of Fe, Cr and Mo, it is very difficult to exactly estimate the real sputter rates. The sputter steps and oxide thicknesses are reported here with respect to SiO_2 without any correction.

3. Results and discussion

The employed direct online coupling of a micro-electrochemical flow cell to ICP-MS has several advantages in respect of sensitivity

and reproducibility of measurements. Due to the small cell diameter, repeated measurements can be performed on the same surfaces even of smaller samples such as the here used melt-spun amorphous ribbons. The obtained time- and element-resolved chemical solution analysis bears great advantages in following specific processes especially for multi-elemental alloys.

The electrochemical behavior of the amorphous $Fe_{50}Cr_{15}Mo_{14}C_{15}B_6$ alloy and of pure Mo and Cr during potentiodynamic experiments was already reported earlier [20]. The amorphous alloy displays a behavior rather similar in some aspects to pure Cr, but modified by the additional constituents (Fig. 1). This suggests that the material breakdown is of similar origin, while pure Mo behaves distinctively different. The amorphous samples show passive behavior with a transformation from a Mo-dominated passive layer at lower potentials to Cr-dominated and Mo-depleted surface layers at elevated potentials. A transpassive material breakdown occurs around 1.1 V_{SHE}, approximately 100 mV lower than pure Cr (Compare here also Fig. 4). The alloy elements enable thus earlier transpassive dissolution, i.e. a distinctive co-dissolution effect. The amorphous alloy shows a significantly higher passive current compared to pure Cr – the value of a few µA is nevertheless still moderate and well comparable with other alloys such as commercial stainless steels. Mo shows transpassive dissolution at much lower potentials that coincide also with the onset of the visible first local peak for the passive alloy. The inset illustrates the irregular atomic arrangement which is typical for the amorphous state and which underlines its chemical homogeneity.

3.1. Influence of gas purging on OCP

To first evaluate the expected spontaneous passivity on the amorphous alloy, OCP measurements were performed under electrolyte gas saturation (air, argon and oxygen) in 0.1 M H_2SO_4. In all cases the OCP value stabilizes within the first few hundred seconds (see for air Fig. 2). Therefore, no significant changes on the surface are observed after this initial time period. The oxygen saturated solution results in the highest OCP value (0.305 V_{SHE}), the argon saturated solution the lowest value (0.16 V_{SHE}). The OCP value measured in aerated electrolyte is around 0.27 V_{SHE}, and thus at the lower end of the passive range close to the transpassive Mo dissolution. The difference to the reversible potential of oxygen is clearly very large. Although transport limitation may also play a role, the measured values therefore indicate that the oxygen reduction reaction, which is the only cathodic reaction at this potential,
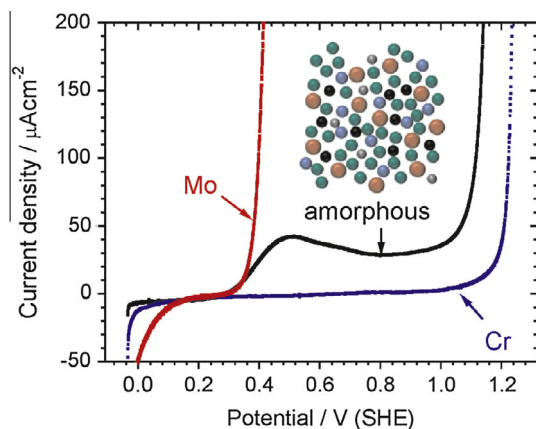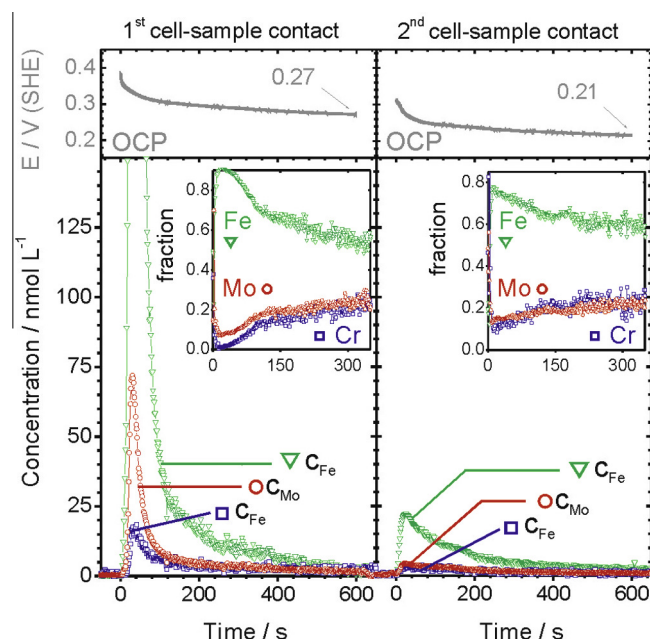

Fig. 2. Initial dissolution profiles at first (left side) cell-sample *contact* and second cell-sample contact (right side) followed by OCP measurements for 600 s for ion milled amorphous $Fe_{50}Cr_{15}Mo_{14}C_{15}B_6$ in aerated 0.1 M H_2SO_4. The concentration of Fe (c_{Fe}) is plotted in green with converse triangles, c_{Cr} in blue squares and c_{Mo} in red dots. OCP is plotted in grey. Electrolyte-sample contact occurred at $t = 0$ s. The inset shows the mole fraction from 0 to 400 s. (For interpretation of the references to color in this figure legend, the reader is referred to the web version of this article.)

is kinetically hindered on the alloy. Furthermore, the values demonstrate that the sample is passive and stable in the used electrolytes and does not undergo pitting. Further electrochemical tests are nonetheless necessary to describe the global corrosion behavior in more detail.

3.2. Initial reaction during first electrolyte contact

A surface reacts on changes of surface potential as well as on changes of the environment leading to a new equilibrium or steady-state. When a metal surface is brought into contact with the electrolyte, possible reactions might be active corrosion, selective dissolution, surface film formation or transformations. In the case of alloys, the surface reacts by enrichment or respective depletion of components that are more or less stable in the new environment. The behavior at the initial contact of the amorphous $Fe_{50}Cr_{15}Mo_{14}C_{15}B_6$ alloy with aerated 0.1 M H_2SO_4 at OCP is shown in Fig. 2. The figure shows the dissolution profiles and OCP measurements over time for 600 s after an initial cell-sample contact (1st cell-sample contact, Fig. 2, left) and after a second cell-sample contact at the same position (Fig. 2, right). The corresponding OCP values are presented above the dissolution profiles. Fig. 2 demonstrates how the dissolution profile is altered on a surface that has been contacted with electrolyte before.

The ICP-MS measurement is continuous and runs with sustained electrolyte flow also when the coupled SFC is lifted from the working electrode surface. This allows recording the background baselines of the elements at $t < 0$. At $t = 0$ s the cell-electrolyte contact occurs when the cell is pressed onto the sample surface while the OCP measurement is started with establishing the closed circuit after contact with electrolyte. For the first, initial cell-sample contact the measured OCP value in air-saturated electrolyte (Fig. 2) stabilized within the first few hundred seconds at around 0.27 V_{SHE} indicating no further significant surface changes

Fig. 1. Potentiodynamic polarization behavior of an amorphous $Fe_{50}Cr_{15}Mo_{14}C_{15}B_6$ alloy, pure Mo and Cr in 0.1 M H_2SO_4 with a scan rate of 2 mV s^{-1}. The data is shown here as an overview and was adapted from Ref. [20]. The inset illustrates the structure of the amorphous alloy.

within the observed time interval. After cell lift-off and re-contacting, a small shift in the OCP is visible for the second cell-sample contact, with a final value of then 0.21 V_{SHE}. In both cases a high dissolution rate appears in the beginning, which however decreases after a few seconds. The peak intensity is much stronger for the first cell-sample contact. Comparing the measured concentration for individual elements along all samples, the main element dissolved is Fe in amounts higher than expected from the respective bulk stoichiometry, while Cr and Mo dissolve under-stoichiometric and thus accumulate on the surface.

To quantify the relation between all dissolved species, the peaks were numerically integrated between 0 and 200 s and the values (nmol s L^{-1}) multiplied with the flow rate (3.85 µL s^{-1}) to yield the total amount (shown in pmol) of metal dissolved. The results are summarized in Table 1.

The total amount of metal ions dissolved in the time period (0–200 s) at second cell-sample contact is much lower as the protective film has already formed (Table 1). The main species dissolved during the initial period is Fe in both cases, but the ratio is different: while the amount of dissolved Fe accounts for 86% during the first contact, it is 70% after the second contact. Cr and Mo dissolve first with 4% and 10%, respectively, and after the second contact with 13% and 16%, respectively.

During the first cell-sample contact Fe dissolves over-stoichiometrically causing a surface enrichment of Mo and Cr at the hold potential. The dissolution profile approaches a low-level steady state, as expected for spontaneous passivation. The tailing and peak broadening in the ICP-MS data are typical phenomena originating from the electrolyte flow system [5]. Similar to processes in chromatography setups axial or eddy molecular diffusion lead to broadening phenomena [24], and temporary adsorption in the involved tubing causes a slow decay or tailing of residual signals possibly depending on the specific elements. In the present case, the initial dissolution originates from the transformation of an ultrathin native film into an electrolyte-grown passive film. This spontaneous passivation or spontaneous film transformation at OCP occurs by surface enrichment of Mo and Cr. The film formation and passivation is mostly completed after a period of about 100 s at OCP conditions.

Mo shows slow preferential dissolution during initial electrolyte contact, i.e. Mo acts passivating at this potential, in addition to Cr. This is in agreement with the results from Habazaki [3] who reported passivity of Mo for potentials below 0.4 V_{SHE} (valid for our measured OCP of ~0.27 V_{SHE}), which vanishes when more positive potentials are applied.

The distribution of dissolved species after the second cell-sample contact is, as expected, different from the first contact (see Table 1). In this case, the material dissolves close to the nominal distribution of the elements (63% Fe, 19% Cr and 18% Mo), maintaining the Mo- and Cr surface enrichment. This shows that the changes in the surface film, i.e. the conversion of a native oxide film with a nearly stoichiometric metal content in the film towards an electrolyte-grown passive oxide, occurs at the first electrolyte contact within the first 100 s. This state is then mostly preserved between different contacts.

Assuming a steady-state ion dissolution during the period after the initial dissolution peak has vanished (t > 400 s), it is possible to

calculate the corresponding steady-state current density. The concentration of Mo at t > 400 s with 3 nmol L^{-1} is taken as steady-state concentration, as it shows the highest sensitivity with the lowest limit. By application of Faradays law [5,10] an elemental dissolution current density of 0.3 µA cm^{-2} results for Mo, using a flow rate of 3.85 µL s^{-1}, a charge number of 3, a Faraday constant of 96,485 C mol^{-1} and an area of 0.01 cm^2. By assuming nominal dissolution, the dissolution current densities for Fe and Cr are 0.7 µA cm^{-2} and 0.3 µA cm^{-2}, respectively. Based on these approximations, a total dissolution current density of 1.3 µA cm^{-2} is expected, which fits very well to typical values for passive (stainless) Cr-steels in sulfuric acid [2].

3.3. Element-resolved dissolution monitoring during long term stationary experiments

The steady-state dissolution current densities in the passive range are typically determined using potentiostatic, so-called stationary experiments. Potentio*dynamic* experiments, which are frequently recorded to gain a quick overview of the general corrosion behavior significantly increase the apparent film dissolution rates due to their continuously changing potentials. In addition to charging of the interface capacity also the growth of surface films is not instantaneous and needs time to reach its steady state. The measured ICP-MS concentrations in this case were converted into dissolution current densities by application of Faradays law. Those are labeled $i_{Diss,Me}$ (Me = Fe, Cr, Mo) for the individual metals and $i_{Diss,total}$ for the sum of the former three. For the calculation, the charge number for Fe was assumed to be 2 for potentials below 0.5 V_{SHE} and 3 at 0.8 V_{SHE} and above with a linear transition in between, based on Ref. [25]. A charge number of 3 was used for Cr and 6 for Mo over the whole potential range. This enables to compare the measured current density i_m with the dissolution current densities $i_{Diss,total}$. The mole fraction, i.e. the quotient of one element divided by the sum of all considered elements, was used to describe a dissolution stoichiometry. The here used dissolution stoichiometry refers to the concentration in solution and thus indicates elemental surface enrichment or depletion when compared to the concentration of the bulk material. Stoichiometric dissolution would thus imply nearly equal dissolution of Mo and Cr (14 at.% and 15 at.%, respectively) and dissolution of Fe higher by a factor of 3.3 as its content is 50 at.% in the bulk material.
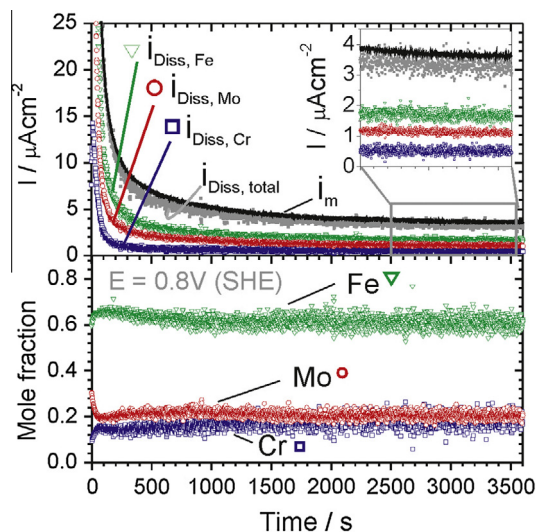
Table 1
Amount of metal ions dissolved at first and second cell-sample contact on an amorphous surface between t = 0–200 s in aerated 0.1 M H_2SO_4.

	1st contact	2nd contact
Fe/pmol	107.3	10.0
Cr/pmol	5.0	1.9
Mo/pmol	12.2	2.3

Fig. 3. Potentiostatic polarization of amorphous sample for 3600 s at 0.8 V_{SHE} in aerated 0.1 M H_2SO_4 and continuous dissolution analysis.

Fig. 3 shows a polarization experiment of an amorphous sample for 3600 s after a potential step from OCP to 0.8 V_{SHE} in 0.1 M H_2SO_4. The potential of 0.8 V_{SHE} was chosen based on potentiodynamic experiments as the potential region where the materials behave passive due to a Cr-based protective film exhibiting a low current density (see Fig. 1). The specimen was initially held at OCP for 600 s (not shown here) followed by the polarization. In principle, $i_{Diss,total}$ follows i_m during the whole time period, i.e. the high current in the beginning decreases within the first hundred seconds. A relatively increased, over-stochiometric Mo dissolution and a slightly under-stoichiometric Cr dissolution become visible in the initial period after the step and extend to about 2000 s at 0.8 V_{SHE}. After reaching steady-state ($t > 2000$ s), a current density of 3.5 $\mu A\,cm^{-2}$ can be observed (Fig. 3). The amorphous sample finally shows stoichiometric dissolution, i.e. Fe dissolves predominantly with Mo and Cr on a lower level. This observation fits to the results obtained from the potentiodynamic sweeps where the amorphous sample dissolves stoichiometrically at potentials higher than 0.7 V_{SHE} [20].

By closer examination, i_m and $i_{Diss,total}$ show a slight deviation, especially at the beginning of the experiment. The deviation can be mainly attributed to oxide growth. Other processes might be possible, e.g. oxidation of boron and carbon, which were not detected by ICP-MS, and also capacitive charging or oxide state changes.

By numeric integration an oxide thickness can be calculated using the following equation:

$$d_{oxide} = \frac{(\sigma_m - \sigma_{Diss})}{z_{oxide} \cdot F} \cdot \frac{M_{oxide}}{\rho_{oxide}} \qquad (1)$$

with ($\sigma_m - \sigma_{Diss}$) as the difference in charge densities (C cm^{-2}, integrals over current density) between electrochemical- and dissolution data, z_{oxide} the charge number which is 6, F the Faraday constant, M_{oxide} being the molar mass and ρ_{oxide} the density of the oxide. We assume a mixed oxide of Fe_2O_3 and Cr_2O_3 with mixed density and mixed molar mass of both species.

The difference in the charge density for the amorphous sample is 1362 $\mu C\,cm^{-2}$ in the time period between 0 and 3600 s. This corresponds to an expected nominal thickness of 0.7 nm or a respective growth of the oxide between 0.3 V_{SHE} and 0.8 V_{SHE}. We note that we do not consider Mo or B here for the estimation of the film thickness. As discussed above, the given potential is within the transpassive regime for Mo species and we therefore do not expect a major content of Mo within the ultrathin passive film. Another small deviation may result from a boron content in the film which nevertheless is expected to follow the small overall content in the alloy.

3.4. Stepwise stationary experiments

Fig. 4 shows several potentiostatic step experiments in anodic direction on the amorphous sample in aerated 0.1 M H_2SO_4 solution. The potential was stepwise increased by 100 mV for periods of 600 s each, starting from 0.1 V_{SHE} to 1.1 $V_{SHE,}$ which corresponds to the potential range of the sweep experiment (see Fig. 1). The dissolution profile and dissolution stoichiometry are plotted over time with the potential profile in the middle of the section. At each potential step, a sharp initial increase in current and dissolution is observed, followed by a strong decay. The decay in dissolution indicates an adaption of the passive film, i.e. film growth or structural transformations, in response to the new applied potential. Only at higher potentials close to the breakdown of the passive film by transpassive Cr dissolution the elemental current stays at a high level with no discernible decay. Clearly visible is thus metal dissolution as origin of the increasing current, i.e. a true breakdown of
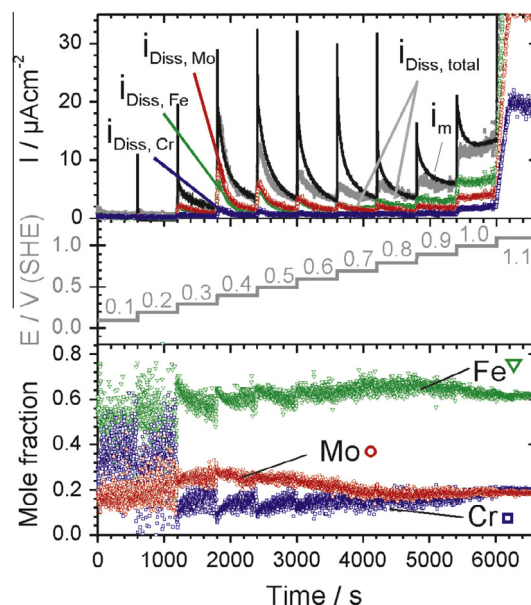

Fig. 4. Dissolution profile and dissolution stoichiometry of amorphous $Fe_{50}Cr_{15}$-$Mo_{14}C_{15}B_6$ alloy during several subsequent potentiostatic polarization experiments in aerated 0.1 M H_2SO_4. All graphs share a common *x*-axis, with the potential profile given in the middle section.

the passive film as corrosion barrier. The onset of transpassive dissolution of the Cr-oxide is related to possible formation of Cr^{6+} ions at the given potential. For all steps, the main species dissolved is Fe. Mo dissolves under-stoichiometric at 0.1 V_{SHE} to 0.2 V_{SHE} as it behaves passive at low potentials and enriches at the sample surface. The current during the anodic potential sweep shows a local maximum at 400–500 mV. In this potential region Mo behaves transpassive and dissolves over-stoichiometrically because the surface has been enriched from polarization in the Mo passive region before. In the case of Cr, the dissolution stoichiometry shows under-stoichiometric Cr-dissolution from 0.3 V_{SHE} to 0.7 V_{SHE}, followed by stoichiometric dissolution of Cr at higher potentials being on the same level with Mo. Clearly, the dissolution stoichiometry and the proceeding of the dissolution current density are affected from both, time and potential-dependent processes, as well as the pre-history of the sample.

During the series of steps, i_m and $i_{Diss,total}$ deviate at the beginning of each step but converge within the run due to a partial contribution of capacitive interface charging and oxide growth. As a technical side remark also occasional electrolyte leaks at the contact point can occur, and would be visible in a continuous deviation of i_m and $i_{Diss,total}$ as the ions dissolved outside the cell are effectively not detected in the upstream ICP-MS. Typically the measured dissolution currents, however exhibit a very high reproducibility. Moreover, the sample is under continuous surveillance with high magnification optics. Nevertheless, a slight increase in wetted area invisible for the observer may account for the few $\mu A\,cm^{-2}$ of minor inaccuracy in the measurement.

3.5. Step experiments in anodic and cathodic direction

In the previous section potentiostatic steps only in anodic direction were presented. Fresh film formation, but also temporal partial or complete dissolution and re-formation are nevertheless frequent in corrosion processes. Beside the dissolution behavior during an stepwise increase of the potential in anodic direction, different step directions may thus be instructive [11]. For stainless steel samples, the fundamental reaction during cathodic polariza-
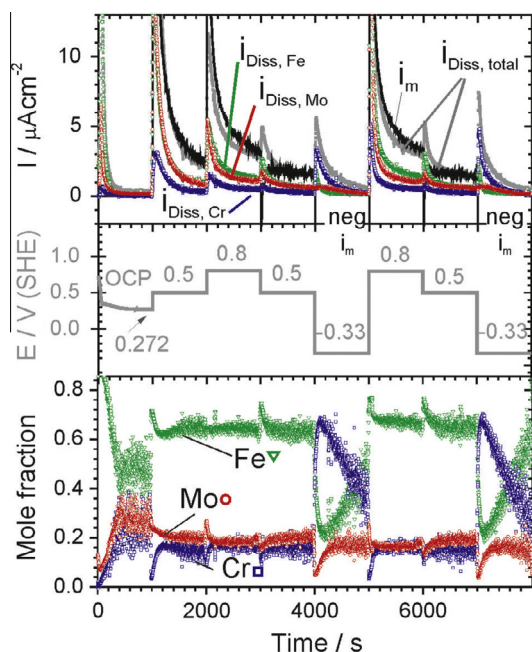
Fig. 5. Dissolution profile and dissolution stoichiometry of amorphous $Fe_{50}Cr_{15}$-$Mo_{14}C_{15}B_6$ alloy during several subsequent potentiostatic polarization experiments in Argon saturated 0.1 M H_2SO_4. All graphs share a common x-axis, with the potential profile given in the middle section.

tion is the reduction of Cr(III) to soluble Cr(II) species. The ultrathin passive film is consequently dissolved enabling an active Fe dissolution. Fig. 5 shows the results from multiple potential-step experiments on an amorphous sample in Argon saturated 0.1 M H_2SO_4 solution. The measurement is following a potential profile with anodic and cathodic steps with intervals of 1000 s each, as shown in the middle section of Fig. 5. The dataset displays a very good agreement between several steps of the measured total electrical current densities i_m and the total dissolution current densities $i_{Diss,total}$.

In the initial OCP period, the surface adapts to the electrolyte as discussed in the previous section. It shows the typical under-stoichiometric Cr and Mo-dissolution. The following potential step to 0.5 V_{SHE} displays the expected initial over-stoichiometric Mo dissolution in conjunction with Cr-enrichment. This Mo dissolution is enlarged by the former surface enrichment in Mo during the OCP period. Consequently, over-stoichiometric Mo dissolution is only observed at the two anodic potential steps following the OCP period. Interesting to note is the cathodic potential step between 0.8 and 0.5 V_{SHE}. The total electrical current density i_m starts at negative values and increases in time within the step to around 2 $\mu A\,cm^{-1}$. Since the potential decreases, no additional oxide is formed. Rather the surface oxide adjusts to the new, lower steady-state thickness [26–28]. Given a continuous, potential independent dissolution of the oxide film, this would imply that reformation of the film stops until the new thickness is reached. However, a dissolution peak and a clear increase in Fe dissolution is seen. At the same time both, Cr and Mo, are under-stochiometrically dissolved i.e. further accumulated in the surface film. A different level of Mo is thus incorporated in the passive film at different potentials. The observations also underline the hypothesis that a potential change in the oxide film always involves material dissolution, probably by reorganization of the surface layer. Capacitive (de)charging with a large non-faradaic contribution should thus explain the observed dip in the total electrical current. A clear separation of both effects, oxide growth and capacitive charging, is not possible at this point. Similar to the previous

section, the elemental dissolution decreases from the first potential step to 0.5 V_{SHE} and the second, due to the dominating rearrangement at 0.8V_{SHE} in between.

After applying a cathodic step to −0.33 V_{SHE}, an overall moderate dissolution peak is observed. An initially large fraction of Cr is dissolved due to the reduction of Cr(III) to soluble Cr(II) species, as seen in the mole fraction displayed in Fig. 5. The contribution of Mo is initially very low and reaches values according to the bulk stoichiometry within about 200 s. In contrast the adaption of the stoichiometry for Cr and Fe takes more than 1000 s. Also during cathodic steps and associated (partial) oxide reduction a (limited) metal dissolution occurs for the alloy. The cathodic, reductive steps in Fig. 5 are here in comparison relatively large. The respective (negative) current density is, as we focus on the respective (positive) metal dissolution, out of scale, indicated by "neg i_m" in the Figure. The onset of metal dissolution during reductive processes was also shown by some of the present authors to be relevant in catalytic systems, in particular Pt [6]. When applying again 0.8 V_{SHE} the entire system quickly readjusts within 200 s and reaches steady-state stoichiometric dissolution.

3.6. Step pulse experiments in cathodic and anodic direction

In order to address spontaneous passivation and adaption processes, a relaxation experiment was conducted in Argon saturated 0.1 M H_2SO_4 solution. The amorphous sample was first polarized cathodically for 60 s at −0.4 V_{SHE}, followed by a period at OCP and then an anodic polarization for 60 s in the passive range at 0.8 V_{SHE} again followed by an OCP period. Fig. 6 clearly shows that the total dissolution signal decays quickly after both, the cathodic and anodic step, which illustrates that spontaneous passivation or respective film adaption proceeds very rapidly in 100–200 s. The OCP, as visible in the middle section, rapidly converges to the steady-state value of 0.27 V_{SHE} after both steps. This includes a thickening or thinning of the surface oxide depending on what potential was previously applied and an adaption of the film composition. The cathodic pulse is associated with an excess dissolu-
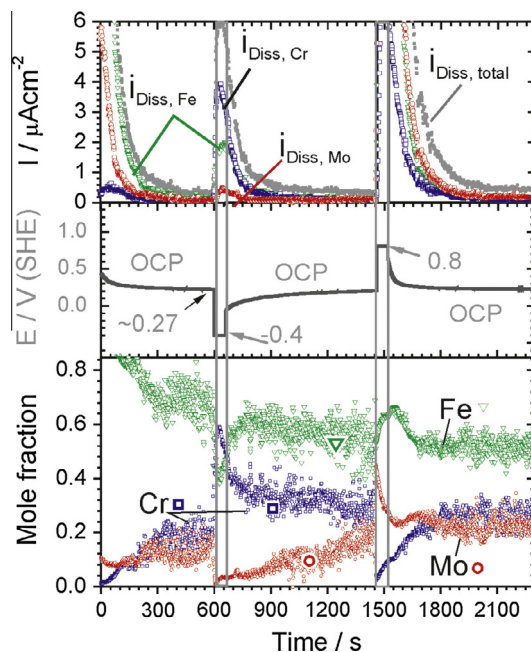

Fig. 6. Cathodic and anodic polarization pulses for 60 s followed by an OCP period for amorphous specimen in Argon saturated 0.1 M H_2SO_4. All graphs share a common x-axis, with the potential profile given in the middle section.

tion of Cr due to the reduction of Cr(III) to soluble Cr(II). Only minor dissolution is observed for Mo. Releasing the sample to OCP, the dissolution drops off markedly. After the anodic pulse, the dissolution is significantly stronger due to the strong dissolution of Fe and Mo, which prolongs the signal decay due to tailing of the SFC measurements. The dissolution fractions during OCP periods appear strongly different in their time-dependent behavior after the cathodic or anodic step.

The data presented support the assumption of spontaneous passivation of the amorphous material. Even after the cathodic pulse the material returns back in its passive state with strongly decreasing dissolution during the OCP period. The complete compositional adaption of the respective passive film within 600–1000 s takes much longer after the cathodic pulse. As the potential is adjusted faster than the film composition, the top-most surface should have adapted its composition in the same time than the potential and the film interior following more slowly. For comparison to our amorphous system, Ogle et al. [11] transformed for example an austenitic stainless steel sample into a sustainably active state by cathodic activation showing an excess dissolution of Cr and triggered re-passivation by applying anodic potentials.

3.7. X-ray photoelectron spectroscopy

To complement the results from the electrochemical experiments, surface sensitive XPS analysis was performed to investigate the composition, the oxidation state and the oxide thickness of the passive layers formed under different conditions. XPS analysis was carried out on fresh ion milled amorphous samples and on amorphous samples held at OCP for 600 s and samples additionally polarized at 0.8 V_{SHE} for 3600 s in 0.1 M H_2SO_4. In the resulting survey XPS spectra the peaks correspond to O, C, Fe, Cr and Mo. B is only detectable in high resolution detailed spectra. The peaks that were used for fitting are marked in a grey box in the survey spectra shown in Fig. 7.

The surface elemental concentration of amorphous surfaces after ion milling, after OCP measurements for 600 s in electrolyte and after polarization for 3600 s at 0.8 V_{SHE} are shown in Table 2. Obviously, the native oxide film formed on the ion milled surface is different from the passive films formed after electrochemical treatment. Two significant changes occurred: The amount of C is increased and the amount of Fe is decreased for the surfaces after electrochemical treatment. In the case of C, possible reasons might

be a contaminated outer surface due to electrolyte exposure (although the samples were rinsed with ethanol and ultra-pure water), or a preferential segregation of carbon compounds (e.g. carbides) at the outer surface. In the case of Fe, it was already shown that initial electrolyte exposure evokes preferential dissolution of Fe, this phenomenon is also reported in literature [2,21,27]. The amount of O is increased, which indicates an oxide thickening by the electrochemical treatment (considering the ultrathin nature of the formed films). The concentration of Cr is increasing and the amount of Mo is decreasing indicating an enrichment and depletion, respectively.

Further information on the surface films can be obtained from sputter profiles. Fig. 8 shows the respective sputter profiles of an amorphous surface before polarization with a subsequently formed native oxide film and after polarization with a chemically adapted passive surface film. For simplification, only O 1s, Mo 3d, Fe $2p_{3/2}$ and Cr $2p_{3/2}$ are plotted within the first 5 nm. As expected, the distributions of Fe, Cr, Mo and O in the passive film formed under potentiostatic polarization are different from the native film formed on the surface after ion milling, and show a significant increase in Cr.

The concentration of Fe and Mo in the electrochemically formed passive film is smaller within the first 3.5 nm than in the native oxide, confirming the preferential dissolution of Fe and Mo during polarization as recorded with online ICP-MSICP-MS (Fig. 2). In contrast, the increased concentration of Cr for the polarized surface indicates an enrichment of Cr at the outer layer. These observations are furthermore in a good agreement to other studies on passive films on Fe–Cr alloys and Fe-based metallic glasses [2,21,27]. The enrichment of Cr thereby originates from a preferential dissolution of Fe^{3+} due to the higher initial current density of Fe dissolution from the alloy. Furthermore, the lower mobility of Cr during high field transport through the film causes further accumulation, as suggested by Kirchheim [28].

The concentration of Mo is slightly decreased in the passive film for the polarized sample, which is in full agreement to the electrochemical dissolution stoichiometry at the beginning of the long term experiment (Fig. 3). The ratio of Mo to Cr in the passive film (0.47) is smaller than in the bulk (0.93). Similar results were reported by Hashimoto showing a Mo deficiency in the passive film on Fe–30Cr–2Mo steel after polarization for 3600 s in 1 M HCl [29]. However, oxidized Mo species are found in the film and its beneficial effects are interpreted in terms of a decrease in activity of active surface sites by formation of Mo-oxyhydroxides or Cr- and Fe-molybdates. Habazaki showed an enrichment of Mo for Fe–8Cr–7Mo–13P–7C only in the low potential region where the Cr content is low, whereas no Mo enrichment was found in alloys containing 15% Cr [3]. Accordingly, the addition of Mo improves the passivation ability by assisting the formation of a Cr-enriched passive film and not by forming a passive film itself [3,26,27].

The oxygen concentration decreased significantly within the first nanometer indicating the presence of a very thin surface layer. The ion milled amorphous sample shows an oxide film thickness of around 1.0 nm, the polarized amorphous surface (0.8 V_{SHE} for 3600 s) of around 1.25 nm. Thus the oxide film growth as determined by XPS depth profiles is only 0.25 nm.

Comparing the film thickness for the amorphous surface after polarization quantified by XPS with the film thickness estimated from the dissolution profiles (0.7 nm), the values differ slightly due to the following reasons. First, it is reported in literature that the etch rates of Cr- and Fe-oxides are lower than SiO_2 [23,30], causing in principle an overestimation of the XPS oxide growth from sputter profiles. Secondly, the calculated oxide thickness based on the electrochemical data bears small inaccuracies as the total dissolution current density does not account for dissolution of B and C. The contribution of C to the resulting current is
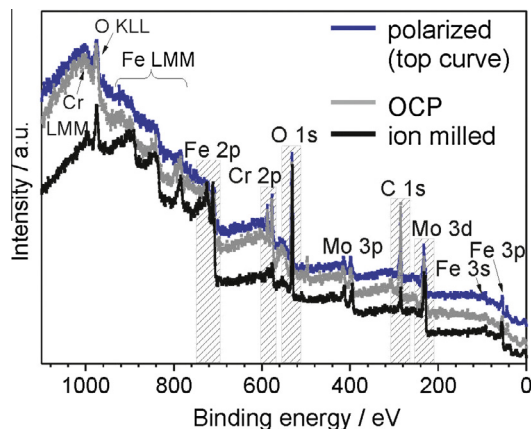

Fig. 7. Xps survey spectra of amorphous $Fe_{50}Cr_{15}Mo_{14}C_{15}B_6$ surfaces (black) fresh ion milled, (grey) held at OCP for 600 s and (blue) polarized for 3600 s at 0.8 V_{SHE} in aerated 0.1 M H_2SO_4. The major peaks are marked, as well as oxygen present on the surface. The elements used for fitting are highlighted in a grey dashed box. (For interpretation of the references to color in this figure legend, the reader is referred to the web version of this article.)

Table 2
Surface elemental atomic concentrations obtained from a XPS survey spectra of amorphous surfaces of Fe after ion milling, after OCP for 600 s and after polarization for 3600 s at 0.8 V_{SHE} in aerated 0.1 M H_2SO_4.

Element	Ion milled surface (at.%)	OCP (at.%)	Polarized for 3600 s at 0.8 V_{SHE} (at.%)
O 1s	42	44	48
Fe 2p	21	5	3
Cr 2p	6	7	8
Mo 3d	7	6	4
C 1s	24	38	37
B 1s	<2	<2	<2
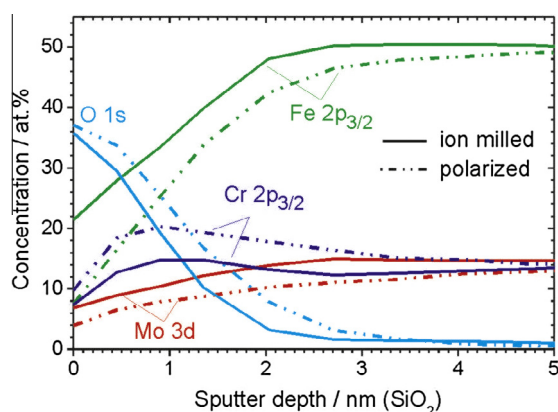
Fig. 8. XPS sputter profiles of ion milled amorphous surfaces of $Fe_{50}Cr_{15}Mo_{14}C_{15}B_6$ before (continuous line) and after polarization at 0.8 V_{SHE} for 3600 s in aerated 0.1 M H_2SO_4 (dashed line). Only Fe $2p_{3/2}$, Cr $2p_{3/2}$, and Mo 3d and O 1s are plotted within the first 5 nm.

expected to be very low. It could be shown for B that it is present in its oxidized form on the sample surface and therefore taking part in the electrochemical process. This assumption is supported by findings from Heusler on $Fe_{80}B_{20}$ alloys [31]. When assuming the dissolution of B, with a charge number of 3, in a similar manner as the dissolution of Fe in the ratio that corresponds to bulk composition (ratio 1:8), i_m and $i_{Diss,total}$ will narrow the estimated thickness from 0.7 nm to 0.35 nm. Further possible inaccuracies might stem from an increase of the surface area due to a roughening by electrochemical treatment. A roughness factor >1 would lower the difference integral between i_m and $i_{Diss,total}$ (see Eq. (1)) and reduce the thickness. The accompanying charging of the electrodes (Helmholtz layer and space charge layer) may also cause an experimental error and overestimation of oxide formation. Finally, also a possible alteration of the film by the ion beam during sputtering may take place, which is a well-known problem of ion beams [32–34] and electron beams [35] interacting with complex surface films. Despite the discussed inaccuracies and the well-known challenges of nanoscale film analysis the different independent techniques yield comparable results with similar quantitative numbers.

As the passive film formed during polarization is enriched in Cr at the outer layer (see sputter profiles in Fig. 8), the chemical state of the metals, especially the one of Cr can reveal key information [36]. High resolution detailed spectra of Cr $2p_{3/2}$ can be fitted into a metallic component (574.2 eV) and into an oxidic and hydroxidic component (576.0 eV and 577.3 eV, respectively). Also the signal of Fe can be divided into one metallic component and into oxidic Fe^{2+} and Fe^{3+} components, and the Mo signal shows besides metallic parts oxidic Mo^{4+} and Mo^{6+} species (not shown).

The comparison of the surface before and after Ar sputtering shows, as expected, that the metallic part increases while the oxidic and hydroxidic species decrease. As an example, in Fig. 9a the distributions of metallic and of combined oxidic and hydroxidic

parts of the Cr $2p_{3/2}$ peak for an amorphous surface before and after polarization are plotted as function of the sputter depth. Within the first nanometer, i.e. within the passive film, the oxidic fraction strongly exceeds the metallic one. During polarization this oxidic fraction clearly increases. Furthermore, a detailed analysis of the O 1s peak shows a significantly higher contribution of OH^- species at the outer surface, while the native surface is primarily composed of O^{2-} species (Fig. 9b). It can therefore be confirmed that the passive film formed in the electrolyte under electrochemical treatment is mainly composed of hydroxides and oxyhydroxides (detailed spectra are not shown here), which is also well known in literature [2,29,37].

One more aspect to briefly discuss besides the metallic constituents is the behavior and role of C in the passive layer. With 15 at.% the carbon content in the studied alloy is remarkably high, and largely differs from classical stainless steels (C < 1%, typically below 0.15%). It can be assumed that carbon is not oxidized electrochemically, but it might affect metal-ion mobility and accumulate or deplete within the passive film. From the survey spectra a strong increase in the carbon content is visible due to electrochemical treatment (see Table 2). From sputter profiles of surfaces before and after electrochemical treatment (Fig. 10a) a strong enrichment of C at the outer layer is visible which diminishes after the first sputter step. The amount of C is only slightly increased within the material depth. High-resolution spectra show a main C—C peak and a carbide peak, and additionally C—O and C=O peaks at higher binding energy before sputtering on both the ion milled and polarized surface. After sputtering only a main carbide peak and a small C—C peak can be found (Fig. 10b and c), confirming the presence of carbide species on both surfaces as already found by XRD and APT previously. The high amount of C in the first step can be attributed to contamination at the outer surface.

4. Conclusions

Multi-element resolved corrosion analysis was successfully followed by online coupling of an ICP-mass spectrometer to a micro-electrochemical scanning flow cell. We demonstrated the application of online ICP-MS coupling to an electrochemical corrosion study of an ultimately homogeneous, amorphous $Fe_{50}Cr_{15}Mo_{14}C_{15}B_6$ alloy. The partial dissolution rates of Fe, Cr and Mo as function of time were compared to the measured total electrical current density. The deviation between dissolution and total current density could be attributed to charging of the interface capacity and to oxide growth. An oxide thickness was estimated to be below 0.7 nm, or 0.35 nm considering the influence of B. Complementary XPS analysis of polarized amorphous samples show an enrichment of Cr at the outermost layer mainly consisting of Cr oxides. The increase in oxide thickness between the native and the polarized amorphous surface is 0.25 nm according to XPS and agrees reasonably well with the oxide thickness obtained from the ICP-MS data. The amorphous alloy shows spontaneous passivation. Within electrolyte contact the native surface film transforms into a passive film with preferential Fe dissolution leading to an enrichment of
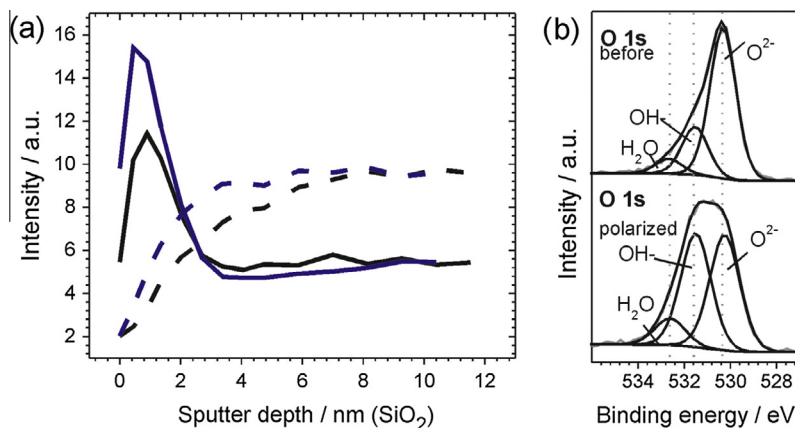
Fig. 9. (a) Distribution of metallic and oxidic parts of Cr $2p_{3/2}$ as function of the sputter depth for the amorphous surface before and after polarization (0.8 V_{SHE}, 1000 s, aerated 0.1 M H_2SO_4), (b) O 1s peak of an amorphous surface before and after polarization at 0 nm sputter depth (0.8 V_{SHE}, 1000 s, aerated 0.1 M H_2SO_4).
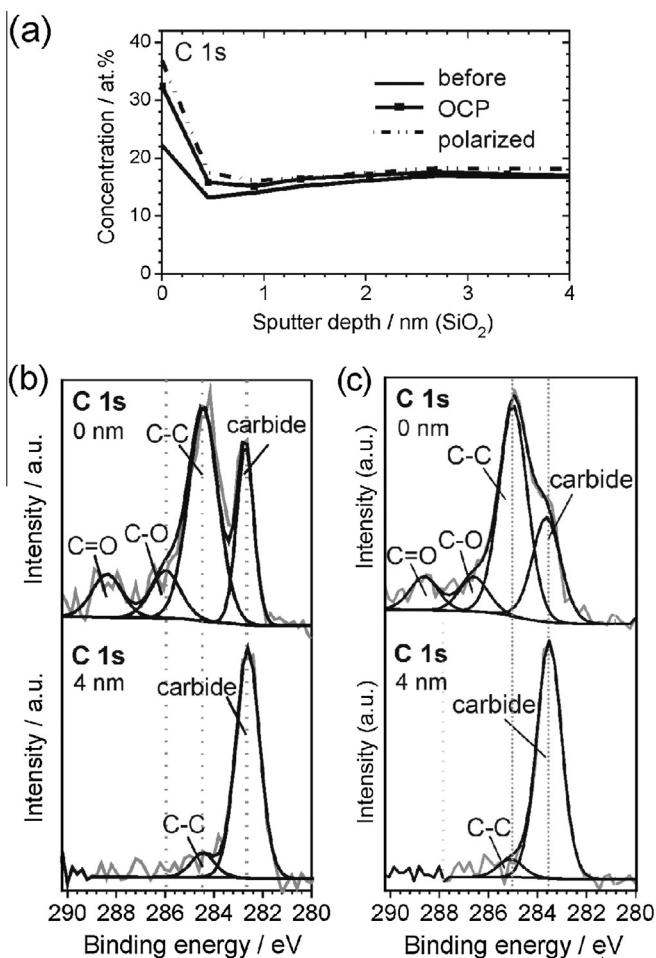

Fig. 10. (a) XPS sputter profile for C only of amorphous surfaces before electrochemical treatment, after OCP for 600 s and after polarization (3600 s at 0.8 V_{SHE}) in aerated 0.1 M H_2SO_4. (b) C 1s high resolution detailed spectra of native amorphous surface before and after 4 nm Ar sputtering. (c) C 1s high resolution detailed spectra of polarized amorphous surface before and after 4 nm Ar sputtering.

3.5 $\mu A\,cm^{-2}$. Furthermore, we reported detailed time-resolved passive film formation in combination with elemental dissolution behavior for several more complex potential step sequences, which provide further insights into the adaption of the surface to different applied potentials, i.e. environmental conditions.

References

[1] K. Hashimoto, W.R. Whitney, Award lecture: in pursuit of new corrosion-resistant alloys, Corrosion 58 (2002) 715–722.
[2] R. Kirchheim, B. Heine, H. Fischmeister, S. Hofmann, H. Knote, U. Stolz, The passivity of iron–chromium alloys, Corros. Sci. 29 (1989) 899–917.
[3] H. Habazaki, A. Kawashima, K. Asami, K. Hashimoto, The corrosion behavior of amorphous Fe–Cr–Mo–P–C and Fe–Cr–W–P–C alloys, Corros. Sci. 33 (1992) 225–236.
[4] A. Pardo, M.C. Merino, A.E. Coy, F. Viejo, R. Arrabal, E. Matykina, Pitting corrosion behaviour of austenitic stainless steels – combining effects of Mn and Mo additions, Corros. Sci. 50 (2008) 1796–1806.
[5] S.O. Klemm, A.A. Topalov, C.A. Laska, K.J.J. Mayrhofer, Coupling of a high throughput microelectrochemical cell with online multielemental trace analysis by ICP-MS, Electrochem. Commun. 13 (2011) 1533–1535.
[6] A.A. Topalov, I. Katsounaros, M. Auinger, S. Cherevko, J.C. Meier, S.O. Klemm, J.C. Meier, S.O. Klemm, K.J.J. Mayrhofer, Dissolution of platinum: limits for the deployment of electrochemical energy conversion?, Angew Chem. Int. Ed. 51 (2012) 12613–12615.
[7] G.N. Ankah, A. Pareek, S. Cherevko, A.A. Topalov, M. Rohwerder, F.U. Renner, The influence of halide additives on the initial anodic dissolution of Cu_3Au (1 1 1), Electrochim. Acta 85 (2012) 384–392.
[8] J. Castle, J. Qiu, The application of ICP-MS and XPS to studies of ion selectivity during passivation of stainless-steels, J. Electrochem. Soc. 137 (1990) 2031–2038.
[9] N. Homazava, A. Ulrich, U. Krähenbühl, Spatially and time-resolved element-specific in situ corrosion investigations with an online hyphenated microcapillary flow injection inductively coupled plasma mass spectrometry set-up, Spectrochim. Acta 63 (2008) 777–783.
[10] S.O. Klemm, J.-C. Schauer, B. Schuhmacher, A.W. Hassel, A microelectrochemical scanning flow cell with downstream analytics, Electrochim. Acta 56 (2011) 4315–4321.
[11] K. Ogle, M. Mokaddem, P. Volovitch, Atomic emission spectroelectrochemistry applied to dealloying phenomena II. Selective dissolution of iron and chromium during active–passive cycles of an austenitic stainless steel, Electrochim. Acta 55 (2010) 913–921.
[12] M. Valtiner, K. Kristiansen, G.W. Greene, J.N. Israelachvili, Effect of surface roughness and electrostatic surface potentials on forces between dissimilar surfaces in aqueous solution, Adv. Mater. 23 (2011) 2294–2299.
[13] K. Kristiansen, M. Valtiner, G.W. Greene, J.R. Boles, J.N. Israelachvili, Pressure solution – the importance of the electrochemical surface potentials, Geochim. Cosmochim. Acta 75 (2011) 6882–6892.
[14] E. Casero, C. Alonso, J.A. Martin-Gago, F. Borgatti, R. Felici, F. Renner, T.L. Lee, J. Zegenhagen, Nitric-oxide adsorption and oxidation on Pt(1 1 1) in electrolyte solution under potential control, Surf. Sci. 507–510 (2002) 688–694.

Mo and Cr on the surface. Mo is passive at the OCP (∼0.27 V_{SHE}) and becomes transpassive at higher potentials, which results in a further transformation of the low-potential Mo-rich passive film into a Cr-rich Mo-depleted film at elevated potentials. The passive sample at 0.8 V_{SHE} shows a steady-state current density of

[15] M. Oezaslan, F. Hasché, P. Strasser, Pt-based core–shell catalyst architectures for oxygen fuel cell electrodes, J. Phys. Chem. Lett. 4 (2013) 3273–3291.

[16] A. Inoue, Stabilization of metallic supercooled liquid and bulk amorphous alloys, Acta Mater. 48 (2000) 279–306.

[17] M. Archer, C. Corke, B. Harji, The electrochemical properties of metallic glasses, Electrochim. Acta 32 (1987) 13–26.

[18] C. Suryanarayana, A. Inoue, Iron-based bulk metallic glasses, Int. Mater. Rev. 58 (2013) 131–166.

[19] S.J. Pang, T. Zhang, K. Asami, A. Inoue, Bulk glassy Fe–Cr–Mo–C–B alloys with high corrosion resistance, Corros. Sci. 44 (2002) 1847–1856.

[20] M.J. Duarte, J. Klemm, S.O. Klemm, K.J.J. Mayrhofer, M. Stratmann, S. Borodin, A.H. Romero, M. Madinehei, D. Crespo, J. Serrano, S.S.A. Gerstl, P.P. Choi, D. Raabe, F.U. Renner, Element-resolved corrosion analysis of stainless-type glass-forming steels, Science 341 (2013) 372–376.

[21] P. Marcus, I. Olefjord, A round robin on combined electrochemical and AES/ESCA characterization of the passive films on Fe–Cr and Fe–Cr–Mo alloys, Corros. Sci. 28 (1988) 589–602.

[22] Z.M. Wang, Y.T. Ma, J. Zhang, W.L. Hou, X.C. Chang, J.Q. Wang, Influence of yttrium as a minority alloying element on the corrosion behavior in Fe-based bulk metallic glasses, Electrochim. Acta 54 (2008) 261–269.

[23] D.R. Baer, M.H. Engelhard, A.S. Lea, P. Nachimuthu, T.C. Droubay, J. Kim, B. Lee, C. Mathews, R.L. Opila, L.V. Saraf, W.F. Stickle, R.M. Wallace, B.S. Wright, Comparison of the sputter rates of oxide films relative to the sputter rate of SiO, J. Vac. Sci. Technol. Vac. Surf. Films 28 (2010) 1060–1070.

[24] J.J. van Deemter, F.J. Zuiderweg, A. Klinkenberg, Longitudinal diffusion and resistance to mass transfer as causes of nonideality in chromatography, Chem. Eng. Sci. 5 (1956) 271–289.

[25] S. Haupt, H. Strehblow, A combined surface analytical and electrochemical study of the formation of passive layers on FeCr alloys in 0.5 M H$_2$SO$_4$, Corros. Sci. 37 (1995) 43–54.

[26] I. Olefjord, B. Brox, U. Jelvestam, Surface composition of stainless steels during anodic dissolution and passivation studied by ESCA, J. Electrochem. Soc. 132 (1985) 2854–2861.

[27] C.O.A. Olsson, D. Landolt, Passive films on stainless steels - chemistry, structure and growth, Electrochim. Acta 48 (2003) 1093–1104.

[28] R. Kirchheim, B. Heine, S. Hofmann, H. Hofsäss, Compositional changes of passive films due to different transport rates and preferential dissolution, Corros. Sci. 31 (1990) 573–578.

[29] K. Hashimoto, M. Naka, K. Asami, T. Masumoto, An X-ray photoelectron spectroscopy study of the passivity of amorphous Fe–Mo alloys, Corros. Sci. 19 (1979) 165–170.

[30] Sputtering by Particle Bombardment, in: R. Behrisch, W. Eckstein (Eds.), Topics in Applied physics 110, Springer Verlag, Berlin Heidelberg, 2007.

[31] S. Kapusta, K.E. Heusler, Corrosion of the glassy metals Fe80B20 and Fe40Ni40B20, Z. Für. Met. 72 (1981) 785–791.

[32] T.J. Chuang, C.R. Brundle, K. Wandelt, An X-ray photoelectron spectroscopy study of the chemical changes in oxide and hydroxide surfaces induced by Ar$^+$ ion bombardment, Thin Solid Films 53 (1978) 19–27.

[33] R. Steinberger, J. Duchoslav, M. Arndt, D. Stifter, X-ray photoelectron spectroscopy of the effects of Ar ion sputtering on the nature of some standard compounds of Zn, Cr, and Fe, Corr. Sci. 82 (2014) 154–164.

[34] E. Lewin, M. Gorgoi, F. Schäfers, S. Svensson, U. Jansson, Influence of sputter damage on the XPS analysis of metastable nanocomposite coatings, Surf. Coat. Technol. 204 (2009) 455–462.

[35] G.T. Burstein, T.P. Hoar, Decomposition of metal oxide films under electron beam bombardment, Corr. Sci. 17 (1977) 939–941.

[36] M.C. Biesinger, B.P. Payne, A.P. Grosvenor, L.W.M. Lau, A.R. Gerson, R. St, C. Smart, Resolving surface chemical states in XPS analysis of first row transition metals, oxides and hydroxides: Cr, Mn, Fe, Co and Ni, Appl. Surf. Sci. 257 (2011) 2717–2730.

[37] M.W. Tan, E. Akiyama, H. Habazaki, A. Kawashima, K. Asami, K. Hashimoto, The role of chromium and molybdenum in passivation of amorphous Fe–Cr–Mo–P–C alloys in deaerated 1 M HCl, Corros. Sci. 38 (1996) 2137–2151.